International Journal of Impact Engineering 90 (2016) 12–25

Contents lists available at ScienceDirect

International Journal of Impact Engineering

journal homepage: www.elsevier.com/locate/ijimpeng

Impact dynamics and puncture failure of pressurized tank cars with fluid–structure interaction: A multiphase modeling approach

Hailing Yu *, David Y. Jeong

Structures and Dynamics Division, Volpe National Transportation Systems Center, U.S. Department of Transportation, 55 Broadway, Cambridge, MA 02142, USA

ARTICLE INFO

Article history:
Received 26 May 2015
Received in revised form 27 October 2015
Accepted 27 November 2015
Available online 9 December 2015

Keywords:
Railroad hazmat tank car shell impact test
Impact dynamics
Puncture failure
Stress triaxiality dependent fracture criterion
Fluid–structure interaction

ABSTRACT

This paper presents a computational framework that analyzes the effect of fluid–structure interaction (FSI) on the impact dynamics and puncture failure of pressurized commodity tank cars carrying hazardous materials. Shell (side) impact tests have been conducted on full scale tank cars resulting in deformed or punctured tank cars. A finite element (FE) modeling method is applied that explicitly simulates the three distinct phases in a tank car loaded with a liquefied substance: pressurized gas, pressurized liquid and solid structure. Furthermore, an equivalent plastic strain based fracture initiation criterion expressed as a function of stress triaxiality is adopted to depict the fracture behavior of the tank car steel material. The fracture initiation is implemented for ductile, shear and mixed fracture modes and followed by further material deterioration governed by a strain softening law. The force, displacement and impact energy results obtained from the FE analysis show good agreement with the corresponding shell impact test data. The simulations demonstrate that FSI plays a critical role in predicting the correct dynamics of tank car impact. The puncture resistance of a tank car, characterized as limit impact conditions in terms of puncture energy or puncture velocity, is further analyzed in shell impact scenarios. The puncture energy is shown to increase as the initial fluid pressure decreases, the tank car thickness increases or the effective impactor size increases. Quantitative correlations between puncture energy/velocity and each of these factors are obtained using the FE analysis method developed in this paper.

© 2015 Published by Elsevier Ltd.

1. Introduction

Pressurized commodity tank cars are commonly employed in the railroad industry to transport liquefied goods including hazardous materials (hazmat) such as compressed flammable (e.g., propane) or toxic gases (e.g., chlorine). In a number of freight train derailment or collision accidents in recent years, severe impacts led to compromised structural integrity of tank cars that consequently released hazmat into the environment. For instance, tank cars loaded with liquefied chlorine were punctured in some accidents by external objects carrying significant momentum; chlorine gas escaped from the breached tank cars, causing respiratory distresses and sometimes fatality among the population exposed to this inhalation hazmat; as a result, affected residential areas were evacuated, and costly environmental cleanup was often needed [1,2]. The railroad hazmat tank cars displayed apparent vulnerability or inadequate protection under the dynamic impact loads in these accidents.

There has been an ongoing research effort aimed at improving the performance of tank cars subjected to dynamic impact loading and thus preventing the puncture failure observed in the aforementioned freight train accidents. A key task has been to determine the puncture resistance of tank cars subjected to impact conditions representative of those in the field. Puncture resistance may be depicted in terms of limit impact conditions, such as minimum initial impact energy or minimum initial impact velocity, to cause puncture failure. For brevity, they are referred to as the puncture energy and the puncture velocity, respectively. To evaluate the puncture resistance of the existing fleet of railroad tank cars and ultimately seek their improved protection, the U.S. government and railroad industry collaborated on a next generation (NextGen) tank car project in which shell impact tests were conducted on full-scale tank cars [3]. Detailed test setup, impact configuration and main outcome of the tests are described in Section 2. In addition to the physical tests, finite element analysis (FEA) was employed throughout the project to provide pretest prediction, posttest evaluation and design guidance [4–6]. In these analyses, simplified representations of the fluid phases (gas and liquid) and their dynamic effects

* Corresponding author. Structures and Dynamics Division, Volpe National Transportation Systems Center, U.S. Department of Transportation, 55 Broadway, Cambridge, MA 02142, USA. Tel.: +1 (617) 494 2554; fax: +1 (617) 494 2113.
E-mail address: hailing.yu@dot.gov (H. Yu).

http://dx.doi.org/10.1016/j.ijimpeng.2015.11.014
0734-743X/© 2015 Published by Elsevier Ltd.

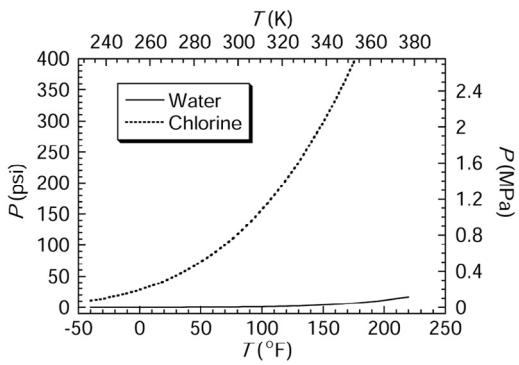

Fig. 1. Vapor pressures of water and chlorine as functions of temperature.

were adopted. Typically, one or both fluid volumes were omitted, and the fluid pressure was simplified as a constant pressure load (equal to the nominal initial fluid pressure) applied directly on a tank car's inner wall. As a result, the interactions between the fluids and the solid structure were not accurately represented in the analyses.

Under normal operating conditions, both liquid and vapor forms of a substance being transported coexist in a tank car. The pressure of a gaseous vapor in dynamic equilibrium with its liquid form at a given temperature is called a vapor pressure. For instance, the Antoine equation calculates the vapor pressure P as a function of the temperature T as follows:

$$\log_{10}(P) = A - B/(T + C) \tag{1}$$

where A, B and C are Antoine coefficients. Based on Eq. (1) and with Antoine coefficients given in reference 7, vapor pressures of water and chlorine are plotted against temperature in Fig. 1. At normal temperatures, the water vapor pressure appears to be negligible, but the chlorine vapor pressure is significant, rendering the chlorine tank cars pressure containers.

Fig. 2 depicts the three interacting phases in a typical chlorine tank car across the longitudinal section: solid structure, liquid and gas. The liquid and gas phases are also referred to as the fluid phases. The fluids transmit pressure onto the tank inner wall, which reacts with balancing internal forces and deflections. Under external impact loading, the tank car structure in the impact zone further responds with elastic–plastic deformations that can be ultimately stretched to a state of failure. Significant structural deformations reduce the volume that the gas occupies and increase its internal pressure, which in turn is imposed upon the tank structure and further affects the structural response. This is a typical fluid–structure interaction (FSI) phenomenon, as the fluid pressure influences the structural response and vice versa.

FSI can have various effects on the dynamics of a closed fluid container, including added fluid mass on the structure; added stiffness to the structure due to fluid pressure; fluid pressure variation with structural deformation; and structural failure. Computational modeling methods have been employed to account for some of these FSI effects in several pressure or non-pressure container applications, such as cargo ship collision, seismic nuclear reactor response and beverage can puncture (e.g., refs. 8–10). In contrast to these applications, the tank car impact problem is unique in that there are two fluid phases in the container and that the fluid pressure is significant enough to affect the structure's susceptibility to failure. As opposed to the simplified fluid modeling approaches adopted in previous tank car studies, this paper presents a multiphase modeling method that addresses all aspects of the FSI effects described above by explicitly modeling all three interacting phases in a tank car: solid structure, pressurized liquid and pressurized gas. Section 3 describes the multiphase FE model development, including constitutive relations, FSI modeling and key FE simulation techniques employed in the study. For the solid phase, in particular, a stress triaxiality dependent fracture initiation criterion, validated with unnotched Charpy impact test data on railroad tank car steel specimens [11–13], was employed to predict the onset of tank car fracture. Section 4 presents the analysis results obtained using the multiphase FE model. The FE model was first validated with the NextGen shell impact test data. The validated model was then used to study the puncture resistance and its dependence on various factors in shell impacts.

It is noted that fluid cavitation can strongly affect FSI in dynamic loading, examples of which were demonstrated in the experimental and numerical studies of marine structures subjected to underwater blast loading [e.g., refs. 14,15]. However, fluid cavitation has not been an observed or reported factor in the impact events of pressurized tank cars. This is partly due to the fact that fluid flow speeds in tank car impact events are considerably lower than those normally associated with cavitation formation. While the duration of a typical underwater blast event was no more than several milliseconds [14,15], the duration of a typical tank car impact event was several hundred milliseconds. This roughly translates into fluid flow speeds that are two orders of magnitude lower in tank car impact than in underwater blast, making it unlikely for low pressure zones to form or cavitation to occur in the former case. In addition, in the tests and FE simulations conducted in this paper, water in the tank cars was pressurized initially to 100 psi (689.5 kPa), a pressure amount significantly higher than the vapor pressure of water at normal temperatures (see Fig. 1). This again deprived the low pressure condition for water to vaporize and form cavitation. For these reasons, no fluid phase transition or cavitation was modeled in this paper.

The Lagrangian formulation was employed to describe both the solid and the fluid domains. In the side impact tests and simulations presented in this paper, there were only small to moderate amounts of fluid sloshing occurring in the tank cars, resulting in moderate fluid mesh deformations. The Lagrangian approach was convenient to implement and sufficient to deal with these deformations and account for the corresponding sloshing effects. More sophisticated alternative methods, such as Arbitrary Lagrangian–Eulerian method and coupling of structural mechanics and fluid dynamics codes, can be considered in cases of significant sloshing (and consequently excessive Lagrangian mesh distortion) but were not necessary in this study.

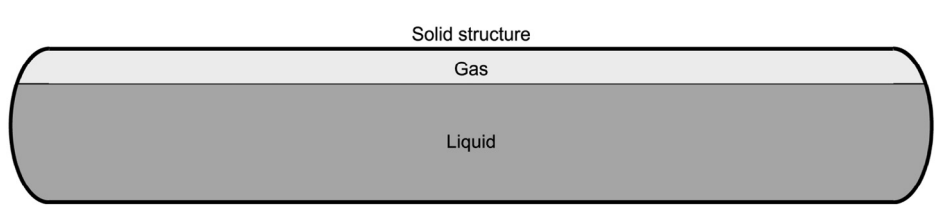

Fig. 2. Illustration of the three interacting phases in a typical chlorine tank car.

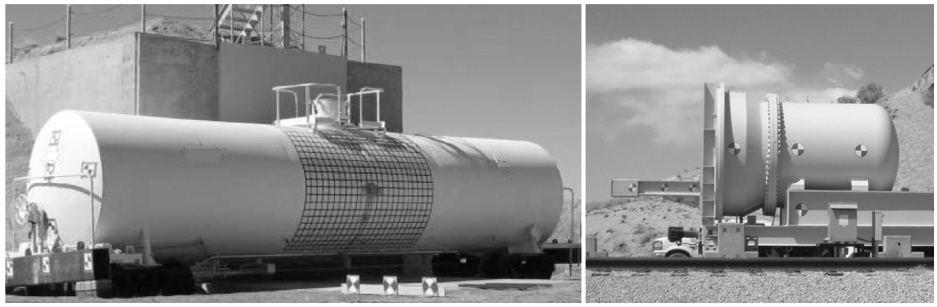

Fig. 3. Typical tank and ram cars employed in full scale shell impact tests.

2. Full scale shell impact tests

The main structure of a tank car consists of two ellipsoidal ends (or heads) connected longitudinally by a cylindrical shell. An object strikes any location on the cylindrical shell in a shell impact scenario and anywhere on the heads in a head impact scenario. Head or shell puncture failure of tank cars was responsible for the chlorine leakage in the freight train accidents described at the beginning of this paper. While many head impact tests had been conducted on full-scale tank cars or individual head components to obtain the force-indentation and puncture characteristics of tank heads [16–19], there had been fewer shell impact tests. To better understand the impact dynamics and puncture resistance of tank shells, three full-scale shell impact tests were conducted in the NextGen tank car project.

Fig. 3 shows the typical tank and ram cars used in the NextGen shell impact tests. For safety, the tank car was filled with water in lieu of liquid chlorine. In addition, water was mixed with clay slurry, and this liquid mixture was made to have the approximate density of liquid chlorine. The liquid mixture occupied 89.4% of the tank volume, whereas air occupied the rest of the tank volume (i.e., 10.6% outage). The air was pressurized initially to $p_0 = 100$ psi (689.5 kPa) to simulate the condition in a tank car loaded with liquid chlorine. The tank car assembly weighed $M_{\text{tank}} = 263$ kips (119 metric tons) with the liquid content, a steel jacket and other accessories. There was a 4 in. (101.6 mm) clearance filled with non-structural insulation materials between the external tank surface and the steel jacket. The tank car assembly was supported by outriggers or skids on the test track. One side of the tank car was placed against a concrete wall, and the other side was exposed to impact from the ram car. The ram car was a ballasted flatcar that weighed $M_{\text{ram}} = 286$ kips (130 metric tons) and had a protruding beam to which an impactor was attached.

After gaining an initial speed v_0 along the impact direction, the ram car made an impactor-first contact with the center of the tank car's shell. The initial impact energy E_0 of the ram car just prior to impact can be calculated as:

$$E_0 = \frac{1}{2} M_{\text{ram}} v_0^2 \tag{2}$$

The impact velocity can be treated as unidirectional because it is significant only along the impact direction, and we used the term "impact velocity" interchangeably with "impact speed" throughout this paper.

Two impactors were employed in these shell impact tests, and their surface geometry is illustrated in Fig. 4. Impactor I had a 17 in. by 23 in. (431.8 mm by 584.2 mm) face whose edges were rounded with a 1 in. (25.4 mm) radius, and Impactor II had a smaller, 6 in. by 6 in. (152.4 mm by 152.4 mm) face and a 0.5 in. (12.7 mm) edge radius. Impactor I is comparable to the cross-section of a coupler shank, and Impactor II is comparable to the cross-section of a draft sill.

Two additional impactors were studied computationally in this paper. Impactor III has a 12 in. by 12 in. (304.8 mm by 304.8 mm) face with a 1 in. (25.4 mm) edge radius, and Impactor IV also has a 12 in. by 12 in. (304. mm by 304.8 mm) face but with a smaller 0.5 in. (12.7 mm) edge radius. Apparently the impact face of Impactor III is geometrically similar to that of Impactor II with a scale factor of 2. Impactor III was employed in a more recent, full scale shell impact test on a tank car shielded by a protective sandwich panel [20]. Impactor IV is hypothetical and was used to study the correlation of the puncture resistance with the effective impactor size. The dimensions of the impactor faces are summarized in Table 1.

Accelerometers were installed on the ram car, and the acceleration data were used to calculate impact forces and impactor displacements. Displacement transducers were mounted on the interior tank wall and provided tank indentation data. No data channel was available to monitor the air pressure.

The test conditions and main results from the two fully instrumented tests (Test 1 and Test 2) are summarized in Table 2. Test 1 was conducted with Impactor I and at an impact velocity $v_0 = 14$ mph (6.26 m/sec); the tank car was dented but otherwise maintained its

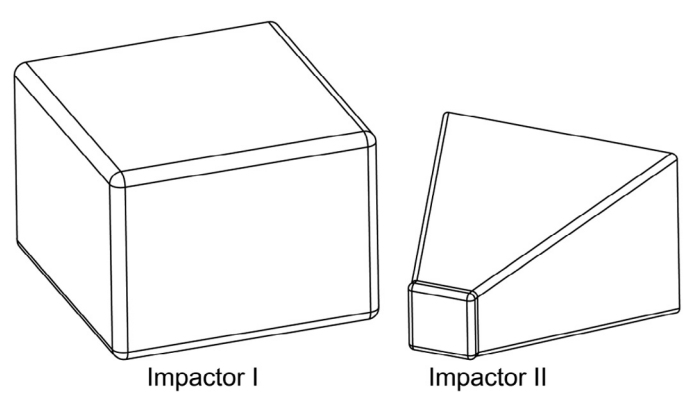

Fig. 4. Schematic of Impactors I and II used in the NextGen full scale shell impact tests.

Table 1
Impactor face dimensions.

Impactor	Height		Width		Edge radius	
	in.	mm	in.	mm	in.	mm
I	17	431.8	23	584.2	1	25.4
II	6	152.4	6	152.4	0.5	12.7
III	12	304.8	12	304.8	1	25.4
IV	12	304.8	12	304.8	0.5	12.7

Table 2
Test conditions and main results from two shell impact tests on full-scale tank cars.

	Test 1	Test 2
Nominal tank car mass M_{tank}	263 kips (119 metric tons)	263 kips (119 metric tons)
Nominal ram car mass M_{ram}	286 kips (130 metric tons)	286 kips (130 metric tons)
Initial fluid pressure p_0	100 psi (689.5 kPa)	100 psi (689.5 kPa)
Impactor	I	II
Initial impact velocity v_0	14 mph (6.26 m/sec)	15.1 mph (6.75 m/sec)
Damage to impact zone	26 in. (0.660 m) deep maximum dent 9 in. (0.229 m) deep residual dent	Punctured
Maximum impact force F_{max}	1292 kip (5747 kN)	887 kip (3946 kN)
Estimated puncture energy E_p	-	0.906 million lbf-ft (1.228 million J)
Estimated puncture velocity v_p	-	9.73 mph (4.35 m/sec)

structural integrity. Test 2 was conducted with Impactor II and at a higher impact velocity $v_0 = 15.1$ mph (6.75 m/sec), resulting in a punctured tank car with escaping fluids. Figs. 5 and 6 show images captured from the video of the tests. Fig. 5 shows the initial impact, indentation and rebound phases observed in Test 1. Fig. 6 shows the initial impact, indentation and puncture phases observed in Test 2. The time histories of impact force, impactor displacement and tank indentation, all along the impact direction, are denoted as $F(t)$, $U(t)$ and $U_{tank}(t)$, respectively, and plotted for both tests in Fig. 7. Two peaks were observed for $F(t)$ obtained from Test 1, whereas only one peak was reached in Test 2 prior to puncture failure (Fig. 7a).

Integration of the F-U cross plot can yield the work W done by the impact force F:

$$W(U) = \int_0^U F(U)dU \tag{3}$$

The minimum impact energy needed to puncture a tank car, or the puncture energy E_p, may be approximately calculated as the work done by the impact force up to the point of perceived puncture failure indicated by an impactor displacement U_p at puncture:

Fig. 5. Images showing initial impact, indentation and rebound phases in Test 1.

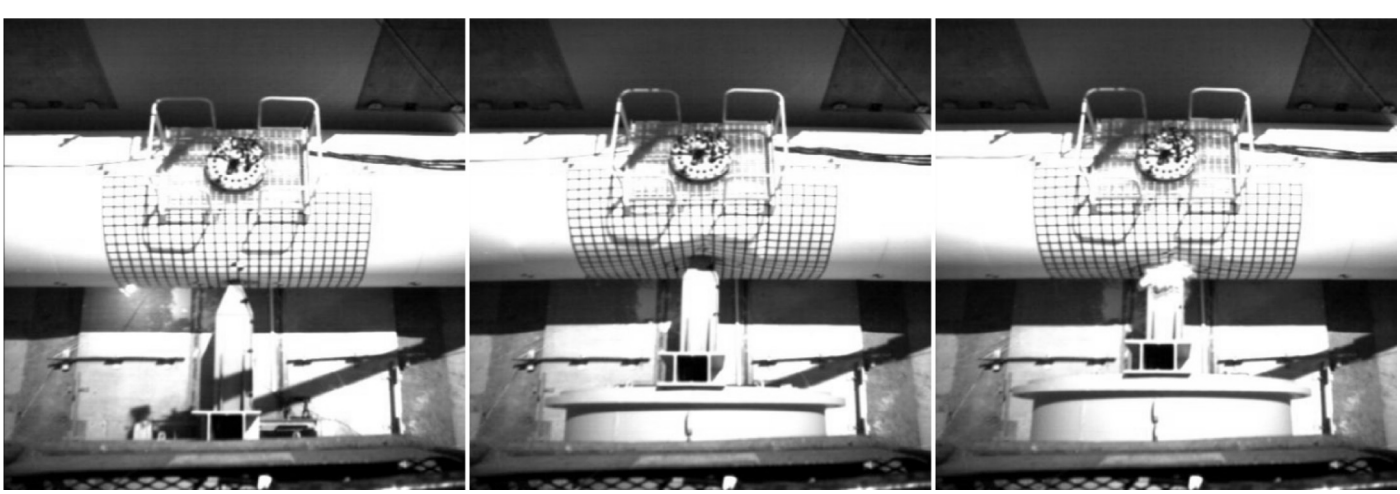

Fig. 6. Images showing initial impact, indentation and puncture phases in Test 2.

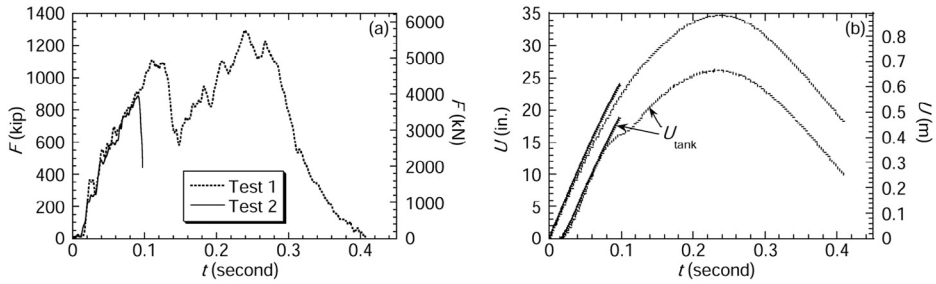

Fig. 7. Impact force $F(t)$, impactor displacement $U(t)$ and tank indentation $U_{tank}(t)$ in Tests 1 and 2.

$$E_p = W(U_p) = \int_0^{U_p} F(U)dU \tag{4a}$$

Alternatively, E_p can be calculated as the lost impact energy by the time puncture occurs:

$$E_p = E_0 - \frac{1}{2}M_{ram}v_r^2 \tag{4b}$$

where v_r is the residual velocity of the ram car upon tank car puncture. The puncture velocity v_p is then determined as:

$$v_p = \sqrt{2E_p/M_{ram}} \tag{5}$$

The puncture energy in Test 2 was estimated to be $E_p = 0.906$ million lbf-ft (1.228 million J) based on Eq. (4), and the puncture velocity was estimated to be $v_p = 9.73$ mph (4.35 m/sec) based on Eq. (5). E_p and v_p could not be estimated for Test 1 as the tank car did not puncture in this test, but they were expected to be higher than those in Test 2 owing to the larger impactor.

The impact dynamics and puncture failure of pressurized tank cars depended on multiple factors including impact condition (impactor dimensions, ram car weight, initial impact velocity, etc.) and tank car configuration (fluid lading, initial fluid pressure, tank car thickness, etc.). The effects of all factors cannot be investigated thoroughly by the experimental method alone. Furthermore, semi-theoretical methods developed to estimate puncture resistance of tank cars depended increasingly on FE simulation results [21,22]. Realistic and accurate FE modeling therefore has become a necessity in tank car impact and puncture studies.

3. Multiphase finite element model

This section describes the governing equations and simulation methods employed in the development of the multiphase modeling approach. This approach was implemented using the commercial nonlinear dynamic FE software Abaqus/Explicit [23].

3.1. Governing equations

3.1.1. Solid structure

The tank car structure is made of specialty steel such as TC-128B. Its behavior can be modeled with elastic–plastic and fracture constitutive relations. The elastic behavior is assumed to be linear and isotropic with Young's modulus E and Poisson's ratio ν. Once the elastic limit is reached, a modified Ramberg–Osgood strain hardening law [24] is observed:

$$\varepsilon = \sigma/E + (\sigma/K)^n \tag{6}$$

where ε and σ are true strain and true stress, respectively, and n and K are material constants dependent on yield and ultimate tensile strengths σ_Y and σ_U. In this study, the calibration of n and K was based on the assumptions that σ_Y corresponds to the 0.2% offset plastic strain and that σ_U corresponds to a total strain of 20%.

As the yield stress evolves to its peak level, fracture or damage is assumed to initiate when the equivalent plastic strain $\bar{\varepsilon}^{pl}$ reaches the fracture initiation strain $\bar{\varepsilon}_0^{pl}$. It is further assumed that $\bar{\varepsilon}_0^{pl}$ depends on the stress triaxiality η:

$$\bar{\varepsilon}_0^{pl} = \bar{\varepsilon}_0^{pl}(\eta) \tag{7}$$

where η is defined as the ratio of the hydrostatic mean stress (σ_m) to the von Mises equivalent stress ($\bar{\sigma}$):

$$\eta = \sigma_m/\bar{\sigma} \tag{8}$$

$$\sigma_m = \frac{1}{3}(\sigma_1 + \sigma_2 + \sigma_3) \tag{9}$$

$$\bar{\sigma} = \sqrt{\frac{1}{2}\left[(\sigma_1-\sigma_2)^2 + (\sigma_2-\sigma_3)^2 + (\sigma_3-\sigma_1)^2\right]} \tag{10}$$

The dependence of $\bar{\varepsilon}_0^{pl}$ on strain rate was not considered. Average strain rate in the impact zone was estimated to be on the order of 10 in./in./sec assuming that an ultimate failure strain of 1.0 in./in. was reached in an impact duration of 0.1 sec. This is consistent with the estimation based on a collision dynamics analysis [25,26]. FE simulation results have further indicated that average strain rates in the impact zone can be an order of magnitude higher than this estimation. Nevertheless, both estimated and FEA predicted average strain rates in tank car impact events fall within a low strain rate range in which the dynamic material behavior of steel is relatively insensitive to strain rate changes [27–29], thus justifying the omission of strain rate effect in modeling.

A plot of the facture initiation strain $\bar{\varepsilon}_0^{pl}$ versus the stress triaxiality η based on Eq. (7) presents a fracture locus of the material under consideration. A fracture locus similar to the one calibrated by Lee and Wierzbicki [30] for industrial aluminum and steel is herein expressed as:

$$\bar{\varepsilon}_0^{pl} = \begin{cases} \infty, & \eta \le -1/3 \\ C_1/(1+3\eta), & -1/3 < \eta \le 0 \\ C_1 + (C_2 - C_1)(\eta/\eta_0)^2, & 0 \le \eta \le \eta_0 \\ C_2\eta_0/\eta, & \eta_0 \le \eta \end{cases} \tag{11}$$

where C_1 is $\bar{\varepsilon}_0^{pl}$ in pure shear ($\eta = 0$) and C_2 is $\bar{\varepsilon}_0^{pl}$ in uniaxial tension ($\eta = \eta_0 = 1/3$). C_2 can be calculated from the reduction in area A_R of a uniaxial axisymmetric tensile specimen as:

$$C_2 = -\ln(1 - A_R) \tag{12}$$

which is also known as the ductility. Further, the hypothesis of a maximum shear stress fracture condition yields C_1 as:

$$C_1 = C_2\left(\frac{\sqrt{3}}{2}\right)^{1/m} \tag{13}$$

where m is the hardening exponent of a power law for isotropic strain hardening, which can be written as:

$$\sigma = K_p \varepsilon^m \tag{14}$$

The strength coefficient K_p and hardening exponent m may be calibrated from the material constants E, σ_Y and σ_U [30].

It is noted that in the original calibration [30,31], η was treated as the average stress triaxiality over a deformation history; in particular, η_0 for uniaxial tension was calibrated to be greater than 1/3. However, $\eta_0 = 1/3$ was adopted in this study as a good approximation of the stress triaxiality at the center section of a uniaxial tensile specimen [32].

A fracture locus depicted by Eq. (11) is plotted in Fig. 8 with three branches: Branch I for ductile fracture due to the mechanism of void nucleation, growth and coalescence; Branch III for shear fracture due to shear band localization; and Branch II for mixed mode fracture. It is noted that with two fixed points $(0,C_1)$ and $(1/3,C_2)$, a fracture locus similar to the Bao–Wierzbicki locus described in Eq. (11) can be obtained by combining the Johnson–Cook criterion for $\eta \geq 1/3$ and the maximum shear stress criterion for $\eta < 1/3$.

The fracture behavior described above was incorporated in the "progressive damage and failure" material model in Abaqus/Explicit [23]. With a predefined fracture initiation criterion expressed in Eq. (7), damage is assumed to initiate upon meeting the following condition:

$$\omega_D = \int \frac{d\bar{\varepsilon}^{pl}}{\bar{\varepsilon}_0^{pl}} = 1 \tag{15}$$

where ω_D is a state variable that increases monotonically with plastic deformation. Eq. (15) indicates that the plastic deformation history is taken into account in determining fracture initiation.

Fig. 9 shows a typical stress–strain curve with which the fracture process starts at $\omega_D = 1$. With this onset of damage, the yield stress softens and the elastic modulus degrades until the equivalent plastic strain reaches its failure limit $\bar{\varepsilon}_f^{pl}$. The damage evolution is monitored by an overall variable D, which is activated upon fracture initiation ($\omega_D = 1$ and $D = 0$) and progresses to $D = 1$ at complete failure. Various damage evolution forms are available, and a linear softening law was adopted for simplicity. Including this post-peak softening behavior was critical to capturing the residual load carrying capability of the ductile steel material beyond the onset of fracture.

To reduce the mesh dependency inherent in softening responses, the fracture energy method originally proposed to model

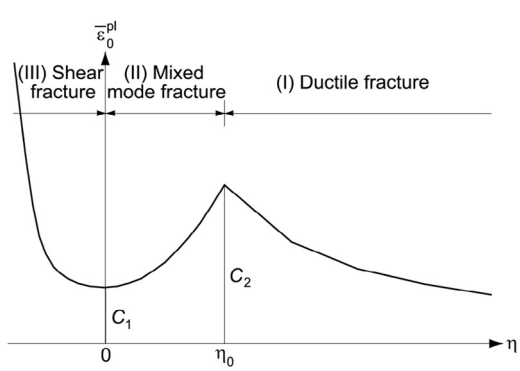

Fig. 8. Three-branch fracture initiation locus for industrial aluminum or steel.

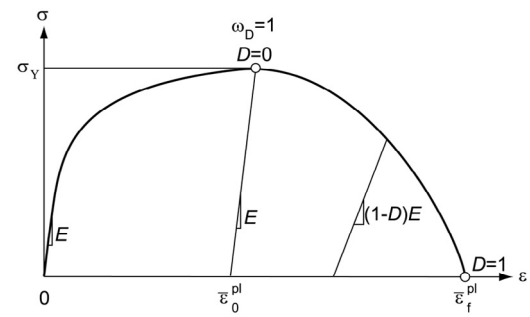

Fig. 9. Typical stress–strain curve showing pre-peak hardening, fracture initiation ($\omega_D = 1$, $D = 0$) and post-peak softening.

the quasi-brittle fracture of concrete [33] was adopted, and the stress–strain relationship was replaced with a stress–displacement relationship for the softening behavior. An equivalent plastic displacement $\bar{u}^{pl}$ is defined that evolves according to the following equation:

$$\dot{\bar{u}}^{pl} = L_e \dot{\bar{\varepsilon}}^{pl} \tag{16}$$

where L_e is an element characteristic length defined as the square root of the integration point area for 2D elements and the cubic root of the integration point volume for 3D elements [23]. Once $\bar{u}^{pl}$ reaches $\bar{u}_f^{pl}$ upon complete failure, elements representing failed material points may be removed. Direct experimental measurement of the parameter $\bar{u}_f^{pl}$ was unavailable, and here it was approximated as the elongation e_L multiplied by the gauge length in uniaxial tensile tests.

3.1.2. Liquid phase

The hydrostatic behavior of the liquid phase can be depicted by equations of state that express the pressure p as a function of the density ρ and the specific energy E_m:

$$p = f(\rho, E_m) \tag{17}$$

where p is positive in compression and E_m measures the internal energy per unit mass. The Mie–Grüneisen equation of state is linear with respect to energy and can be written in the following form:

$$p = f_1(\rho) + f_2(\rho) E_m \tag{18}$$

where $f_1(\rho)$ and $f_2(\rho)$ are model-dependent functions of density. Further, a linear U_s–U_p Hugoniot form of the Mie–Grüneisen equation of state was employed as an effective method to model the behavior of liquids such as water [34]. The initial density ρ_0 and wave speed c_0 are required material parameters from which the elastic bulk modulus is calculated as $\rho_0 c_0^2$.

The deviatoric behavior of the liquid was assumed to be uncoupled from its volumetric response and governed by either a linear isotropic elastic model or a Newtonian viscous fluid model. The shear viscosity served as a penalty parameter to suppress the shear modes that can distort a mesh, and it must be small for the inviscid water.

3.1.3. Gas phase

The gas phase was assumed to follow the ideal gas equation of state:

$$pV = M_{gas} RT \tag{19}$$

where p is the absolute pressure, V is the volume, M_{gas} is the mass, R is the (specific) gas constant and T is the absolute temperature. The gas constant R was a required input. The ideal gas assumption

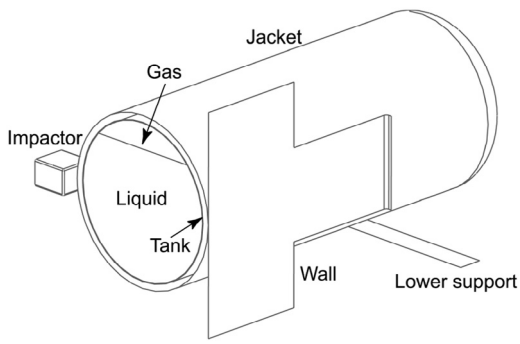

Fig. 10. Typical half symmetric model for the shell impact test of a full scale tank car.

was approximately true for the gas conditions considered. Eq. (19) indicates that without leakage or temperature change, the gas pressure is inversely proportional to the gas volume. It was further assumed that the liquid and gas phases were in dynamic equilibrium and that the temperature was constant throughout the process.

3.2. Model development

The problem domain, boundary conditions and loading conditions were assumed to be symmetric about the tank car center transverse section in the NextGen shell impact tests, so half-symmetric models were developed and illustrated for the simulation of Test 1 in Fig. 10.

A jacket with a 4 in. (101.6 mm) clearance from the exterior tank body was included. In addition to the tank car and its fluid content, Fig. 10 shows a fixed rigid wall (representing the concrete wall) and a rigid lower support (representing the outrigger used in Test 1 or the skid used in Test 2). The lower support was attached to the bottom of the tank assembly. The modeling of the lower support was slightly different for Test 1 than for Test 2 to account for the differences in outrigger and skid supports. A fixed rigid floor not shown in the picture was employed to provide the vertical movement constraint. A rigid body with a lumped mass M_{ram} was attached to the impactor and assigned the same initial velocity as the impactor. The tank accessories were lumped into point masses. The steel material types and nominal geometric dimensions of the tank cars are summarized in Table 3.

3.2.1. Material parameters

The tank car steel material parameters are summarized in Table 4. The liquid and gas material parameters are shown in Table 5. The liquid parameters were based on the properties of water–clay slurry mixture and liquid chlorine, and the gas property was that of air. The coefficient of friction was assumed to be 0.6 for steel-on-steel contacts and 0.3 for the contact between the lower support and the rigid floor.

3.2.2. Fluid–structure interaction

All fluid and solid phases were modeled within the Lagrangian framework. Their interactions were simulated by defining interphase contacts. The gas-to-liquid interface can be modeled with no separation, no slip contact, equivalent to firmly attaching the two materials together along their interface. Alternatively, the two materials can share common nodes along their interface to achieve the same modeling effect while avoiding the contact definition. While the gas-to-liquid contact definition performed well when the entire tank car structure was modeled with shell elements, the “shared nodes” strategy provided more stable contact performance when solid-to-shell coupling was involved (see Section 3.2.4).

To model the fluid-to-solid interactions, smooth contact surfaces were defined where two element types representing the solid phase were joined (see Section 3.2.4). The gas phase has a very low mass, and its contact can be numerically unstable particularly with the shell element type representing the solid structure. Setting the “contact thickness” of the shell elements to zero improved the performance of the gas-to-shell element contact.

Frictionless contact was assumed for all fluid-to-fluid and fluid-to-solid interactions. The frictionless contact defined for a fluid-to-solid interface means slips are allowed in the interface, thus neglecting the effect of a thin fluid boundary layer that observes the “no-slip” condition in the interface. For the overall impact dynamics and puncture resistance responses of tank cars studied in this paper, the effect of these thin layers of “no-slip” fluid boundaries was considered negligible.

3.2.3. Fluid pressure

The initial fluid pressure p_0 was defined as an initial hydrostatic stress state assigned to the fluid elements:

$$\sigma_{11} = \sigma_{22} = \sigma_{33} = -p_0 \tag{20}$$

$$\sigma_{12} = \sigma_{23} = \sigma_{31} = 0 \tag{21}$$

Along fluid-to-solid interfaces, even if we defined exactly matching geometries for the fluid and solid phases, the meshing process can still result in either overclosures or gaps between fluid and solid elements. Mesh overclosures can adversely affect stability and convergence of contact, so we decided to define geometries with sufficiently large initial gaps to completely eliminate mesh overclosures in preprocessing. Once a simulation has started, the initial fluid pressure definition in Eqs. (20 and 21) would allow the

Table 3
Steel material types and nominal geometric dimensions of the tank cars employed in the full scale shell impact tests.

Tank material	Inner diameter		Head thickness		Shell thickness		Shell length		Jacket material	Jacket thickness	
	in.	mm	in.	mm	in.	mm	in.	mm		in.	mm
TC-128B	100.75	2559	0.828	21.03	0.777	19.74	471.47	11,975	ASTM A1011/A569	0.119	3.02

Table 4
Tank car steel material parameters.

Material	ρ		E		ν	σ_Y		n	K		C_1	C_2	$\bar{u}_f^{pl}$	
	lbm/in.^{3}	kg/m^3	ksi	MPa		ksi	MPa		ksi	MPa			in.	mm
TC-128B from Test 1	0.2835	7847	29800	205,465	0.3	55	379.2	10.55	99.15	683.6	–	–	–	–
TC-128B from Test 2	0.2835	7847	31650	218,220	0.3	55	379.2	11.17	96.04	662.2	0.31	1.05	0.32	8.13
ASTM A1011/A569	0.2835	7847	29000	199,949	0.3	30	206.8	9.00	59.85	412.7	0.31	0.92	0.25	6.35

Table 5
Liquid and gas material parameters.

Material	ρ_0		c_0		R	
	lbm/in.^{3}	kg/m^3	in./sec	m/sec	in.^{2}/(sec^2-K)	m^2/(sec^2-K)
Liquid	0.0510	1412	34732.95	882.2	–	–
Gas	–	–	–	–	479034.86	309.05

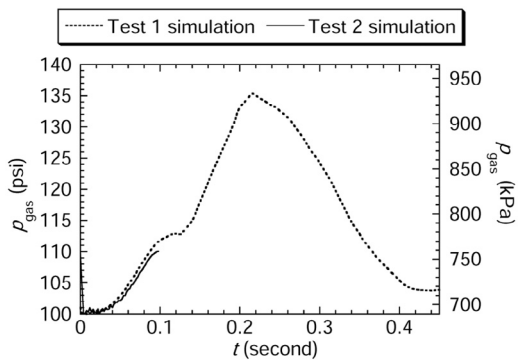

Fig. 11. Average gas pressure $p_{gas}(t)$ obtained from the multiphase simulations of Tests 1 and 2.

fluids to expand and fill the gaps naturally. Consequently the fluids would experience an initial pressure drop at the beginning of the simulation. To mitigate this effect, initial fluid pressures slightly larger than the nominal initial pressure p_0 were usually assigned. The magnitudes of the higher initial pressure depended on individual FE models and were determined from an iterative initialization process.

The time history of fluid pressures can be obtained from the multiphase simulations and averaged over all gas elements to obtain the average gas pressure $p_{gas}(t)$. Fig. 11 shows $p_{gas}(t)$ of air from the simulations of Tests 1 and 2. The average air pressure reached a maximum of 135 psi (930.8 kPa) at about 0.216 seconds in the simulation of Test 1 and a maximum of 110 psi (758.4 kPa) prior to the tank car's puncture in the simulation of Test 2. The maximum air pressure was higher in Test 1 than in Test 2 because the impact event was more prolonged and the larger impactor affected a larger portion of the tank car body in Test 1; both factors led to greater tank deformations which in turn resulted in more significant volumetric changes in the fluids. The peak values in air pressure also indicated that FSI played a more significant role in Test 1 than in Test 2.

3.2.4. Solid-to-shell coupling

The thickness dimension of a tank car is considerably smaller than the other dimensions such as the tank diameter or the tank length. Therefore, the tank car FE models were mostly constructed with shell elements that were accurate and cost effective in simulating the elastic–plastic behavior in the non-impact tank domains. However, for the impact zone in or near contact with the impactor, multi-layered solid elements were employed to capture the progressive damage and ultimate failure behavior through the thickness dimension. To join the solid and shell element domains along their common boundaries, a solid-to-shell coupling technique was employed [23]. Fig. 12 illustrates a typical mesh with multi-layered hexahedral solid elements coupled with shell elements. Note that the shell elements were offset to align with the inner surface of the tank wall represented by the solid elements. This resulted in a smooth inner tank contact surface aimed at improving the contact performance with the fluid elements. The solid elements were fully integrated brick (hexahedron) elements with eight integration points. Based on a mesh sensitivity study conducted in

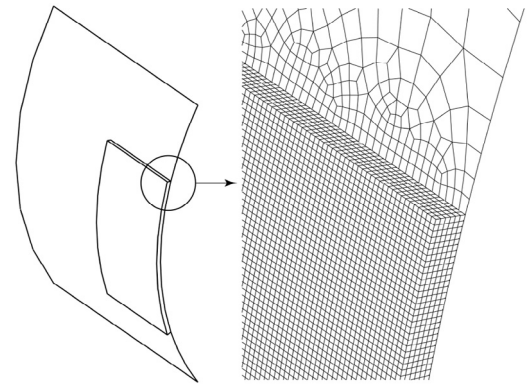

Fig. 12. Illustration of coupled shell and solid elements in the impact zone.

the FEA of unnotched Charpy impact tests [13], six layers of fully integrated brick elements were sufficient to accurately capture the fracture behavior through the typical thicknesses of tank car steel.

To demonstrate the accuracy of the solid-to-shell coupling technique, two simulations, one using solid-to-shell coupling and the other using all shell elements for the tank car structure, were conducted with Test 2 configuration but under an initial impact velocity $v_0 = 9.4$ mph (4.20 m/sec), which did not cause puncture. The resulting impact force $F(t)$ and average air pressure $p_{gas}(t)$ are plotted in Fig. 13. Good agreement was observed between the two sets of simulation results.

4. Results

The multiphase computational model was first validated with the NextGen shell impact test data (Section 4.1). The validated model was then applied to study the puncture energy/velocity and their dependence on various impact conditions and tank car configuration factors (Section 4.2). These simulation results, particularly the quantitative correlation of puncture resistance measures with various engineering factors, can be of great interest to tank car designers/manufacturers, railroad industry, accident investigators, safety regulators and other tank car researchers.

4.1. Validation with test data

In the shell impact test setup, there was a 4 in. (101.6 mm) gap between the concrete wall and the tank exterior surface in the back, while the jacket contacts the concrete wall directly (see Fig. 10). An impact event using this setup can progress in two stages. In Stage I, the impactor/ram assembly pushes the tank toward the concrete wall and continuously reduces the gap between the back of the tank and the jacket. There can be one of two outcomes from Stage I: either the tank car is punctured and the impact event terminates, or the back of the tank comes into direct contact with the jacket against the concrete wall, thus completely eliminating the gap, and the impact event moves on to Stage II. In Stage II, the impactor continues to push the tank against the concrete wall until the tank punctures or the impactor/ram loses all forward momentum and rebounds. Each stage can produce a peak in the impact force $F(t)$. As shown in Fig. 7(a), Test 1 completed both impact stages and the $F(t)$ curve showed two distinct peaks, whereas Test 2 ended with a punctured tank car during Stage I and the $F(t)$ curve showed only one peak.

A simplified fluid modeling approach was examined that omitted the gas phase and applied a constant pressure p_0 on the tank inner wall. Fig. 14 shows the impact force $F(t)$ obtained in Test 1 compared with the FEA prediction using the simplified fluid modeling

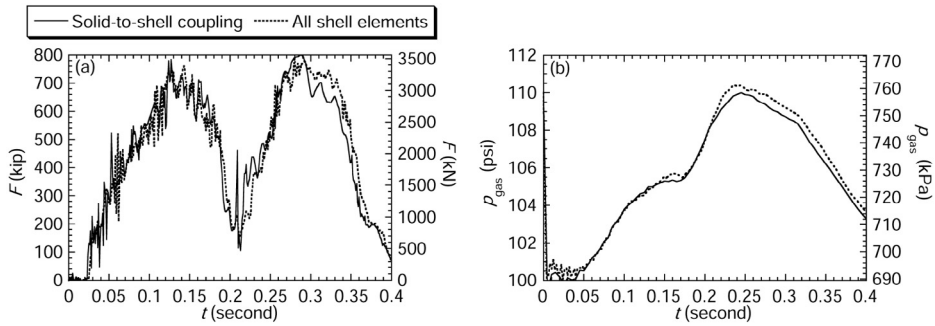

Fig. 13. Impact force $F(t)$ and average gas pressure $p_{gas}(t)$ obtained using solid-to-shell coupling and all shell element tank models with Test 2 configuration and $v_0 = 9.4$ mph (4.20 m/sec).

approach. Three main discrepancies were observed for the $F(t)$ curve produced by the simplified fluid modeling approach as compared to the test data: lower peak force magnitudes, no significant trough or force drop between the two peaks, and lagging of the rebounding impact force in time. Fig. 15 compares the deformed fluid and tank shapes predicted by simplified versus multiphase approaches at different times. The deformations are shown for the symmetric, center transverse cross-section based on the simulations of Test 1. The simplified approach predicted separation of the liquid from the tank inner wall at multiple locations, which was physically unrealistic in pressure containers and can misrepresent the added mass effect by the liquid. Further, the added stiffness effect by the fluid pressure was inaccurate because of the simplified representation of the fluid pressure. The observed discrepancies in the $F(t)$ response were attributed to these combined effects. The simplified fluid modeling approach was also shown to overestimate the tank car puncture resistance [35,36].

Figs. 16 and 17 show the quantitative validation of the simulation results from the multiphase modeling approach with the shell impact test data. Fig. 16 compares the following data for Test 1: impact force $F(t)$ (Fig. 16a), impactor displacement $U(t)$ (Fig. 16b), F-U cross plot (Fig. 16c) and work $W(t)$ done by the impact force based on Eq. (3) (Fig. 16d). Because the tank car did not puncture in Test 1, only shell elements and elastic–plastic material models for the tank car steel were employed in the simulation. This was verified by a check of the equivalent plastic strain (PEEQ) quantity throughout the simulation. The maximum PEEQ for the jacket and the tank car shell were well below the fracture initiation criteria defined in Fig. 8 and Table 4, thus demonstrating that tank car fracture would not have occurred even if failure modeling was employed in the simulation of Test 1. The multiphase approach yielded results that correlated well with the corresponding experimental data. In particular, the multiphase approach significantly improved the prediction of the $F(t)$ curve by modeling the FSI effects more accurately.

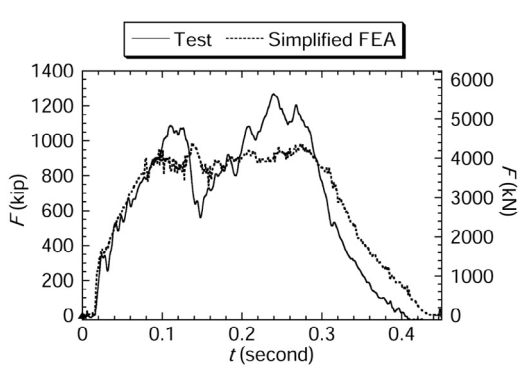

Fig. 14. Test and simplified FEA results on impact force $F(t)$ for shell impact Test 1.

Fig. 17 shows the validation of the multiphase modeling method based on Test 2 data. The simulation of Test 2 applied the progressive damage and failure material model to the solid elements in the tank car's impact zone. A tank car was deemed to lose its structural integrity in a simulation when complete, through-the-thickness element failure was observed at any location in the impact zone, an example of which is shown in Fig. 18. A simulation was discontinued once such a puncture state was observed. Again good agreement between test and simulation results on $F(t)$, $U(t)$, F-U and $W(t)$ curves was observed. The sudden drop in $F(t)$ near 0.1 seconds corresponded to a puncture state being achieved. The multiphase

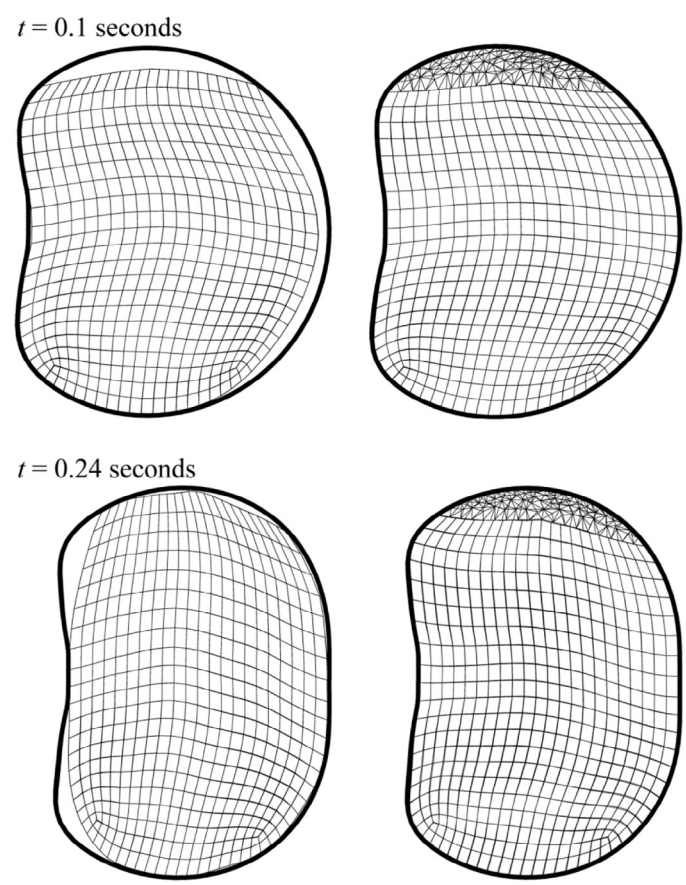

Fig. 15. Deformed fluid and tank shapes in the center transverse section predicted by simplified (left) versus multiphase (right) FEA simulations of Test 1. The hexahedral elements represent the liquid phase. The tetrahedral elements represent the air phase.

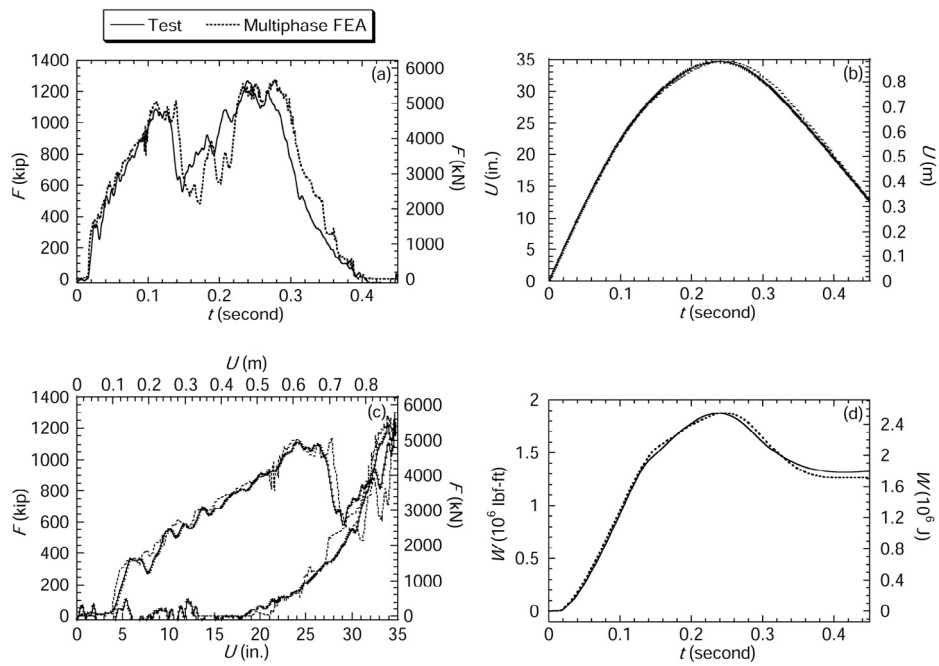

Fig. 16. Test and multiphase FEA results for shell impact Test 1: (a) impact force $F(t)$, (b) impactor displacement $U(t)$, (c) F-U cross plot, and (d) work $W(t)$ done by the impact force.

FEA predicted well both the timing of this event and the maximum force level prior to the tank car puncture.

4.2. Estimation of puncture energy/velocity

A pair of puncture energy E_p and puncture velocity v_p estimations can be made based on the $F(t)$ and $U(t)$ curves and Eqs. (4 and 5). Table 6 shows the estimated E_p and v_p from Test 2 and those from the multiphase simulation of Test 2. Again there was good agreement between the estimations based on the physical test and those based on the multiphase simulation.

The relative difference between the initial impact energy E_0 and the puncture energy E_p was also calculated and shown in the last column of Table 6. There was a nearly 60% difference in E_p relative to E_0 in Test 2, meaning E_0 can be further reduced and still cause puncture in the tank car. The initial impact velocity v_0 was then reduced to 10 mph (4.47 m/sec) in the simulation, which yielded a puncture energy amount identical to the initial impact energy and

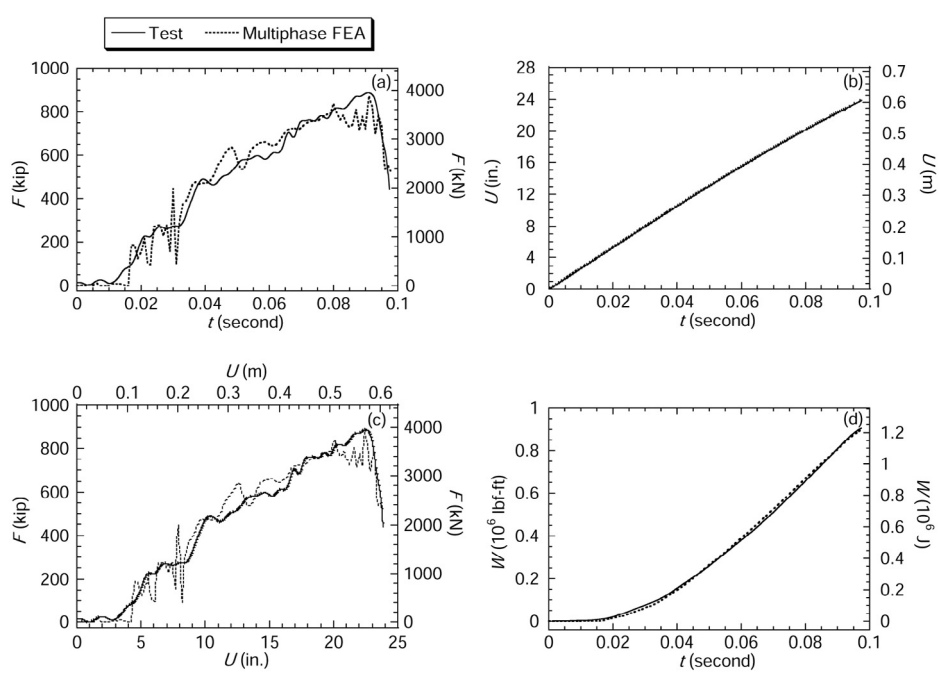

Fig. 17. Test and multiphase FEA results for shell impact Test 2: (a) impact force $F(t)$, (b) impactor displacement $U(t)$, (c) F-U cross plot, and (d) work $W(t)$ done by the impact force.

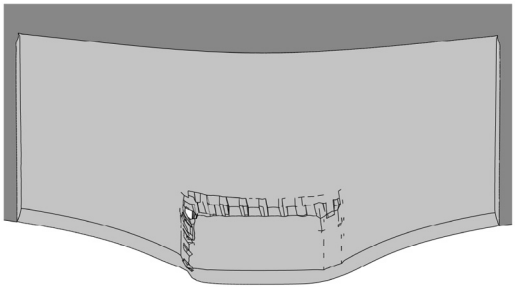

Fig. 18. Illustration of a puncture state with through-the-thickness element failure in the impact zone.

a puncture velocity equal to the initial impact velocity, also shown in Table 6. The $F(t)$ and $p_{gas}(t)$ curves obtained from the simulation are plotted in Fig. 19. The curves are plotted up to the point of tank car failure as defined in Fig. 18. In Fig. 19, the $F(t)$ curve shows two peaks. The $p_{gas}(t)$ curve indicates that at the time of tank car puncture, the average air pressure has decreased from the overall maximum. These facts verified the observation from the simulation that the tank car puncture occurred while the ram car was rebounding during Stage II of the impact.

Table 6 indicates that under Test 2 configuration, the puncture energy/velocity estimations based on the two different initial impact velocities were very similar. However, under other test configurations, there can be larger discrepancies in the puncture estimations using different v_0's. Therefore, the authors proposed a 5% energy difference criterion for acceptable puncture estimations from FE simulations, that is, the estimated puncture energy must be within 5% of the initial impact energy to be acceptable. First an FE simulation is run with tank car puncture being the outcome, and the results are checked against the 5% energy difference criterion; if this criterion is not satisfied, then a new simulation with a reduced initial impact energy amount is run; and this process is repeated until the said criterion is satisfied. If the acceptable puncture energy and puncture velocity estimations are denoted as $\hat{E}_p$ and $\hat{v}_p$, respectively, then the 5% energy difference criterion is expressed as:

$$\hat{E}_p = E_p(E_0, v_0), \quad \text{if } |E_0 - E_p|/E_0 < 5\% \tag{22a}$$

$$\hat{v}_p = \sqrt{2\hat{E}_p / M_{ram}} \tag{22b}$$

4.2.1. Effect of initial fluid pressure

The puncture resistance is believed to increase as the initial fluid pressure p_0 decreases, and a quantitative correlation was sought in this study using the multiphase simulation method described above. In these simulations, the Test 2 configuration was again employed, except that p_0 varied as follows: 150, 100, 50 and 14.7 psi (1.034, 0.689, 0.345 and 0.101 MPa), where $p_0 = 100$ psi (0.689 MPa) corresponded to the exact Test 2 condition, and $p_0 = 14.7$ psi (0.101 MPa) corresponded to the atmospheric pressure condition. The puncture energy/velocity estimations based on the results from these simulations are summarized in Table 7. The simulations that yielded acceptable $\hat{E}_p$ and $\hat{v}_p$ all predicted that tank car puncture occurred when the ram car rebounded during Stage II impact.

The correlation of $\hat{E}_p$ with p_0 is plotted in Fig. 20. The fitted curve was based on a least squares regression analysis. The logarithm function type yielded the best fit, which can be expressed as:

$$\hat{E}_p = 2.7373 - 0.373 \ln(p_0) \tag{23a}$$

where $\hat{E}_p$ is measured in 10^6 lbf-ft and p_0 in psi, or:

$$\hat{E}_p = 1.1958 - 0.505 \ln(p_0) \tag{23b}$$

where $\hat{E}_p$ is measured in 10^6 J and p_0 in MPa. The R^2 coefficient of determination was 0.9848.

4.2.2. Effect of tank car thickness

A tank shell thickness $t_{tank} = 0.777$ in. (19.74 mm) was employed in Test 2. Two additional thicknesses, $t_{tank} = 0.468$ and 0.975 in. (11.89 mm and 24.77 mm), were further studied in multiphase simulations. The corresponding $\hat{E}_p$ and $\hat{v}_p$ estimations are summarized in Table 8. Regression analyses were conducted to correlate $\hat{E}_p$ with t_{tank}, and the exponential function appeared to yield the best fit. The fitted curve can be expressed as:

$$\hat{E}_p = 0.2453 e^{1.874 t_{tank}} \tag{24a}$$

where $\hat{E}_p$ is measured in 10^6 lbf-ft and t_{tank} in in., or:

Table 6
Puncture energy/velocity estimation under the Test 2 configuration.

	v_0		E_0		E_p		v_p		$(E_0-E_p)/E_0$
	mph	m/sec	10^6 lbf-ft	10^6 J	10^6 lbf-ft	10^6 J	mph	m/sec	
Test	15.1	6.75	2.180	2.956	0.906	1.228	9.7	4.35	58.5%
Multiphase simulation	15.1	6.75	2.180	2.956	0.911	1.235	9.8	4.36	58.2%
	10.0	4.47	0.956	1.297	0.956	1.297	10.0	4.47	0.0%

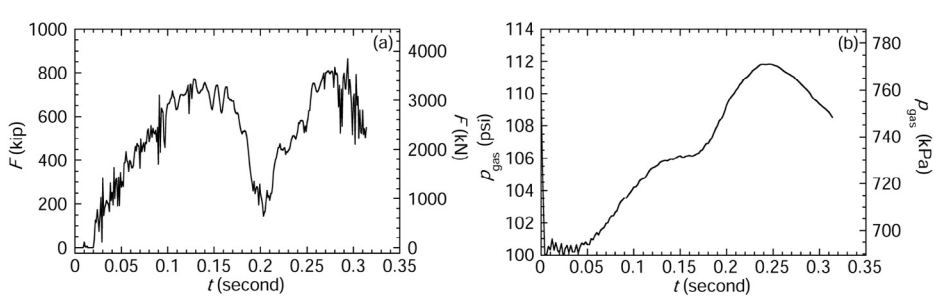

Fig. 19. Impact force $F(t)$ and average gas pressure $p_{gas}(t)$ obtained from multiphase simulation of Test 2 configuration but with an initial impact velocity $v_0 = 10$ mph (4.47 m/sec).

Table 7
Estimated puncture energy and velocity versus initial fluid pressure p_0 (the impact configuration/conditions were otherwise the same as those in Test 2).

p_0		$\hat{E}_p$		$\hat{v}_p$	
psi	MPa	10^6 lbf-ft	10^6 J	mph	m/sec
150	1.034	0.918	1.245	9.8	4.38
100	0.689	0.956	1.297	10.0	4.47
50	0.345	1.287	1.745	11.6	5.19
14.7	0.101	1.743	2.363	13.5	6.04

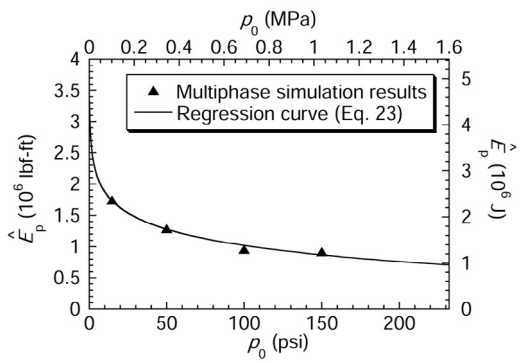

Fig. 20. Correlation of predicted puncture energy $\hat{E}_p$ with initial fluid pressure p_0: multiphase simulation results and regression curve.

Table 8
Estimated puncture energy and velocity versus tank shell thickness t_{tank} (the impact configuration/conditions were otherwise the same as those in Test 2).

t_{tank}		$\hat{E}_p$		$\hat{v}_p$	
in.	mm	10^6 lbf-ft	10^6 J	mph	m/sec
0.468	11.89	0.612	0.830	8.0	3.58
0.777	19.74	0.956	1.297	10.0	4.47
0.975	24.77	1.616	2.191	13.0	5.81

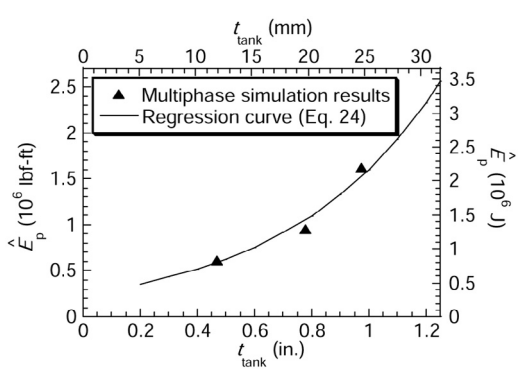

Fig. 21. Correlation of predicted puncture energy $\hat{E}_p$ with tank car thickness t_{tank}: multiphase simulation results and regression curve.

$$\hat{E}_p = 0.3326e^{1.874t_{tank}} \tag{24b}$$

where $\hat{E}_p$ is measured in 10^6 J and t_{tank} in mm. The R^2 coefficient of determination was 0.9706. Both the simulation data and the regression curve are shown in Fig. 21.

4.2.3. *Effect of impactor dimensions*

Additional multiphase simulations were conducted replacing Impactor II in Test 2 with Impactors III and IV (see dimensions in Table 1). The puncture energy/velocity estimations based on these simulations are summarized in Table 9. The first simulation with Impactor III was conducted at $v_0 = 15.2$ mph (6.80 m/sec) and did not show tank car puncture. The second simulation was conducted at $v_0 = 18.0$ mph (8.05 m/sec), and it predicted a puncture velocity $v_p = 15.3$ mph (6.84 m/sec) with a puncture-to-initial energy difference of 28.0%, higher than the 5% acceptance criterion. The final simulation conducted at $v_0 = 16.0$ mph (7.15 m/sec) predicted tank puncture and yielded a puncture energy amount identical to the initial impact energy. The puncture estimation from the final simulation met the 5% energy difference criterion and therefore was accepted. Fig. 22 shows the $F(t)$ and $p_{gas}(t)$ curves obtained from the multiphase simulations using Impactor III. This example demonstrated that the puncture estimations from the second simulation, in which the puncture-to-initial energy difference was not sufficiently small, turned out to be inaccurate.

The impact face of Impactor III was geometrically similar to that of Impactor II with a scale factor of 2 in the length dimension. This increase in impactor size resulted in a 156% increase in $\hat{E}_p$ and a 60% increase in $\hat{v}_p$. Further, Impactor IV's surface had the same length but half the edge radius as those of Impactor III's surface. Table 9 indicates that the use of Impactor IV led to higher puncture energy and puncture velocity as compared to the use of Impactor III. It was further observed from the simulations that the rounded edges of the impactor faces were not in contact with the tank car surface during impact.

Given these observations, effective contact parameters may be calculated from the geometry of an impactor surface excluding the rounded edges. For instance, Impactor III's square surface had a 12 in. (0.3048 m) length and a 1 in. (0.0254 m) edge radius; therefore, the effective length in contact was 10 in., corresponding to an effective contact perimeter of 40 in. (1.016 m) and an effective contact area of 100 in.^{2} (0.0645 m^2). It was postulated that the puncture resistance was directly correlated with the effective perimeter/area of an impactor surface.

Fig. 23 shows the correlation of (a) $\hat{E}_p$ with the effective surface area A and (b) $\hat{v}_p$ with the effective surface perimeter L of the impactor based on the data in Table 9. Both correlations appear perfectly linear. The regression curve for $\hat{E}_p$ versus A is:

$$\hat{E}_p = 0.4651 + 0.0197A \tag{25a}$$

where $\hat{E}_p$ is measured in 10^6 lbf-ft and A in in.^{2}, or:

$$\hat{E}_p = 0.6306 + 41.456A \tag{25b}$$

Table 9
Puncture energy/velocity estimation under the Test 2 configuration with Impactors III and IV.

	v_0		E_0		E_p		v_p		$(E_0-E_p)/E_0$
	mph	m/sec	10^6 lbf-ft	10^6 J	10^6 lbf-ft	10^6 J	mph	m/sec	
Impactor III	15.2	6.80	2.209	2.995	–	–	–	–	–
	18.0	8.05	3.098	4.201	2.232	3.026	15.3	6.84	28.0%
	16.0	7.15	2.448	3.319	2.448	3.319	16.0	7.15	0.0%
Impactor IV	17.3	7.73	2.862	3.880	2.844	3.856	17.2	7.71	0.6%

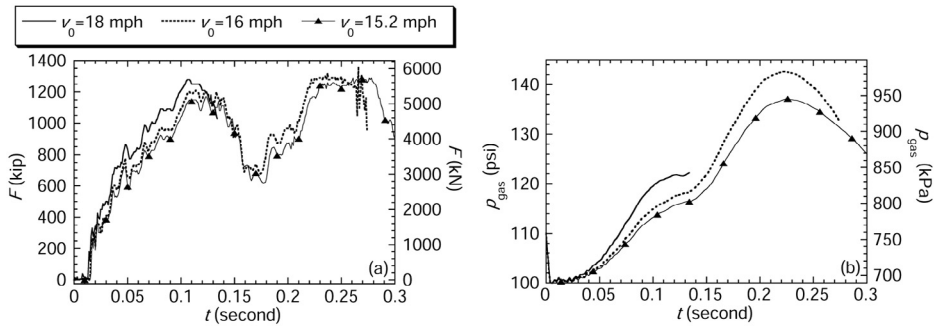

Fig. 22. Impact force $F(t)$ and average gas pressure $p_{gas}(t)$ obtained from multiphase simulations of Test 2 configuration but with Impactor III and varying initial impact velocities.

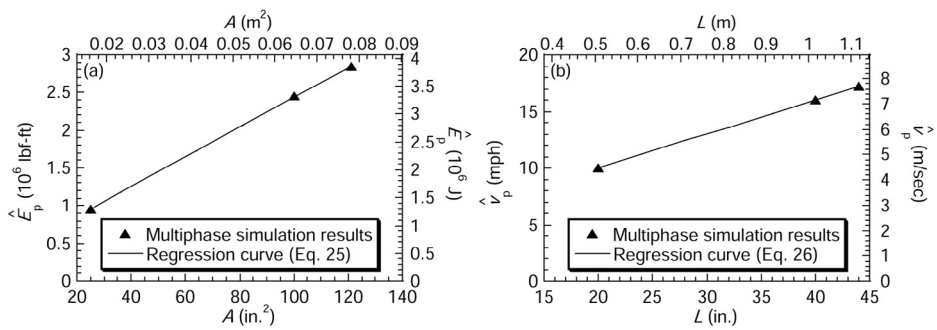

Fig. 23. Correlation of (a) $\hat{E}_p$ with effective surface area A and (b) $\hat{v}_p$ with effective surface perimeter L of the impactor face based on data in Table 9.

where $\hat{E}_p$ is measured in 10^6 J and A in m^2. Eqs. (25) yielded a R^2 of 0.9999.

The regression curve for $\hat{v}_p$ versus L is:

$$\hat{v}_p = 4.0 + 0.3L \tag{26a}$$

where $\hat{v}_p$ is measured in mph and L in in., or:

$$\hat{v}_p = 1.7882 + 5.28L \tag{26b}$$

where $\hat{v}_p$ is measured in m/sec and L in m. Eqs. (26) yielded a perfect correlation with $R^2 = 1$.

4.2.4. *Effect of ram car weight*

The ram car mass M_{ram} was increased from 286 to 572 kips (130 to 259 metric tons) in the multiphase simulation under Test 2 configuration except with Impactor III. The puncture energy/velocity estimations under the two M_{ram} cases are summarized in Table 10. The puncture velocity $\hat{v}_p$ was much lower with the higher ram car mass. Furthermore, the puncture energy $\hat{E}_p$ decreased by 14.7% as M_{ram} doubled, indicating that it would take less energy to puncture a tank car with a larger ram mass.

Table 10
Estimated puncture energy and velocity versus ram car weight (under Test 2 configuration except for the employment of Impactor III).

M_{ram}		$\hat{E}_p$		$\hat{v}_p$	
kip	Metric ton	10^6 lbf-ft	10^6 J	mph	m/sec
286	130	2.448	3.319	16.0	7.15
572	259	2.089	2.832	10.5	4.67

5. Conclusions and discussion

A multiphase FE simulation method was developed in this paper to simulate the interactions among the solid and fluid phases in an impacted tank car. The method was implemented in the Lagrangian framework of a commercial FE program and showed improved predictions of the impact dynamics and puncture failure of pressure tank cars over a simplified method that did not fully account for the FSI effects. The force, displacement and work time histories predicted by the multiphase method agreed well with the available full scale shell impact test data.

Used in conjunction with a stress triaxiality dependent fracture initiation criterion for the tank car steel material, the multiphase method predicted the limit impact conditions to cause puncture in terms of (minimum) puncture energy and (minimum) puncture velocity. It was observed that the predicted puncture energy/velocity depended on the initial impact velocity employed in a simulation, thus an iterative simulation process was devised to determine the actual minimum energy/velocity to cause puncture.

Multiphase analyses indicated that the puncture energy increased as the initial fluid pressure decreased, the tank car thickness increased or the effective impactor size increased. The computational method was able to provide quantitative correlations between puncture energy/velocity and each of these factors. Based on limited simulation data, it appears that less impact energy is needed to puncture a tank car using a larger ram car mass.

Acknowledgements

The Federal Railroad Administration's Office of Research and Development sponsored the research presented in this paper. Mr. Francisco Gonzalez is the FRA project manager for research on rail-

road tank cars. The full-scale shell impact tests described in this paper were funded and conducted by the Next Generation Rail Tank Car Project which was sponsored by Dow Chemical Company, Union Pacific Railroad, and Union Tank Car Company. FRA participated in this project through a Memorandum of Cooperation.

References

[1] National Transportation Safety Board. Collision of Union Pacific Railroad Train MHOTU-23 with BNSF Railway Company Train MEAP-TUL-126-D with Subsequent Derailment and Hazardous Materials Release. Macdona, Texas, June 28, 2004, Railroad Accident Report NTSB/RAR-06/03; 2006.
[2] National Transportation Safety Board. Collision of Norfolk Southern Freight Train 192 with Standing Norfolk Southern Local Train P22 with Subsequent Hazardous Materials Release at Graniteville. South Carolina January 6, 2005, Railroad Accident Report NTSB/RAR-05/04; 2005.
[3] Tyrell DC, Jeong DY, Jacobsen K, Martinez E. Improved Tank Car Safety Research. Proceedings of the 2007 ASME Rail Transportation Division Fall Technical Conference, RTDF2007-46013, September 2007.
[4] Tang YH, Yu H, Gordon JE, Priante M, Jeong DY, Tyrell DC, et al., Analysis of Full-Scale Tank Car Shell Impact Tests. Proceedings of the 2007 ASME Rail Transportation Division Fall Technical Conference, RTDF2007-46010, September 2007.
[5] Tang YH, Yu H, Gordon JE, Jeong DY, Perlman AB. Analysis of Railroad Tank Car Shell Impacts Using Finite Element Method. Proceedings of the 2008 IEEE/ASME Joint Rail Conference, JRC2008-63014; 2008.
[6] Kirkpatrick SW. Detailed Puncture Analyses of Various Tank Car Designs. Final Report for the Next Generation Rail Tank Car (NGRTC) Project, Applied Research Associates, Inc, Mountain View, California; 2009.
[7] National Institute of Standards and Technology. NIST Chemistry WebBook. NIST Standard Reference Database Number 69, <http://webbook.nist.gov/chemistry/>; 2015.
[8] Zhang A, Suzuki K. A comparative study of numerical simulations for fluid-structure interaction of liquid-filled tank during ship collision. Ocean Eng 1997;20:173–84.
[9] Sigrist JF, Broc D, Lainé C. Dynamic analysis of a nuclear reactor with fluid-structure interaction: part I: seismic loading, fluid added mass and added stiffness effects. Nucl Eng Des 2006;236:2431–43.
[10] Yoon JW, Cardoso RPR, Dick RE. Puncture fracture in an aluminum beverage can. Int J Impact Eng 2010;37:150–60.
[11] Yu H, Jeong DY, Gordon JE, Tang YH. Analysis of impact energy to fracture unnotched Charpy specimens made from railroad tank car steel. Proceedings of RTDF2007, ASME Rail Transportation Division Fall Technical Conference; 2007.
[12] Jeong DY, Yu H, Gordon JE, Tang YH. Finite element analysis of unnotched Charpy impact tests. Materials Science & Technology Conference and Exhibition; 2008.
[13] Yu HL, Jeong DY. Application of a stress triaxiality dependent fracture criterion in the finite element analysis of unnotched Charpy specimens. Theor Appl Fract Mech 2010;54:54–62.
[14] Wei X, Tran P, de Vaucorbeil A, Ramaswamy RB, Latourte F, Espinosa HD. Three-dimensional numerical modeling of composite panels subjected to underwater blast. J Mech Phys Solids 2013;61(6):1319–36.
[15] Schiffer A, Tagarielli VL. The one-dimensional response of a water-filled double hull to underwater blast: experiments and simulations. Int J Impact Eng 2014;63:177–87.
[16] Phillips EA, Olsen L. Final Phase 05 Report on Tank Car Head Study. RPI-AAR Tank Car Safety Research and Test Project, Report RA-05-1-17; 1972.
[17] Lishaa M, Chen J, Yang JCS, Kao R, Orth C. Impact of projectile of elliptical tank head. Pressure Vessel and Piping Conference, ASME; 1985.
[18] Coltman M, Hazel M. Chlorine Tank Car Puncture Resistance Evaluation. Final Report, DOT/FRA/ORD-92/11; 1992.
[19] Larson WG. Aluminum/Cold Temperature Tank Car Puncture Resistance Tests: Data Report. Final Report, DOT/FRA/ORD-92/29; 1992.
[20] Carolan ME, Jeong DY, Perlman B, Murty YV, Namboodri S, Kurtz R, et al. Application of Welded Steel Sandwich Panels for Tank Car Shell Impact Protection. Final Report, DOT/FRA/ORD-13/19; 2013.
[21] Jeong DY, Tang YH, Yu H, Perlman AB. Engineering Analyses for Railroad Tank Car Head Puncture. Proceedings of ASME International Mechanical Engineering Congress and Exposition, IMECE2006-13212, 2006; 2006.
[22] Jeong DY, Tang YH, Perlman AB. Semi-Analytical Approach to Estimate Railroad Tank Car Shell Puncture. ASME/ASCE/IEEE 2011 Joint Rail Conference, JRC2011-56028; 2011.
[23] Dassault Systèmes. ABAQUS analysis user's manual; 2012.
[24] Ramberg W, Osgood WR. Description of stress-strain curves by three parameters. Technical Note No. 902, National Advisory Committee for Aeronautics; 1943.
[25] McKeighan PC. Mechanical Properties of Tank Car Steels Retired from the Fleet. Southwest Research Institute Report to Volpe National Transportation Systems Center, August 2008.
[26] McKeighan PC, Jeong DY, Cardinal JW. Mechanical properties of tank car steels retired from the fleet. Proceedings of ASME Joint Rail Conference; 2009. pp. 235–44.
[27] Zener C, Hollomon JH. Effect of strain rate upon plastic flow of steel. J Appl Phys 1944;15(1):22–32.
[28] Campbell JD, Ferguson WG. The temperature and strain-rate dependence of the shear strength of mild steel. Phil Mag 1970;21(169):63–82.
[29] Yu S-S, Lu Y-B, Cai Y. The strain-rate effect of engineering materials and its unified model. Lat Am J Solids Struct 2013;10(4):833–44.
[30] Lee Y-W, Wierzbicki T. Quick fracture calibration for industrial use, Report No: 115. Impact & Crashworthiness Laboratory, Massachusetts Institute of Technology; 2004.
[31] Bao Y, Wierzbicki T. On fracture locus in the equivalent strain and stress triaxiality space. Int J Mech Sci 2004;46:81–98.
[32] Earl JC, Brown DK. Distribution of stress and plastic strain in circumferentially notched tension specimens. Eng Fract Mech 1976;8:599–611.
[33] Hillerborg A, Modeer M, Petersson PE. Analysis of crack formation and crack growth in concrete by means of fracture mechanics and finite elements. Cem Concr Res 1976;6:773–82.
[34] Dassault Systèmes. ABAQUS benchmarks manual; 2012.
[35] Yu H, Tang YH, Gordon JE, Jeong DY. Finite element analysis of fluid-structure interaction in pressurized tank cars subjected to dynamic impact loading. Proceedings of SIMULIA Customer Conference, London, United Kingdom, May 2009.
[36] Yu H, Tang YH, Gordon JE, Jeong DY. Modeling the effect of fluid-structure interaction on the impact dynamics of pressurized tank cars. Proceedings of ASME International Mechanical Engineering Congress & Exposition, November 2009.